International Journal of Heat and Mass Transfer 52 (2009) 5922–5931

Contents lists available at ScienceDirect

International Journal of Heat and Mass Transfer

journal homepage: www.elsevier.com/locate/ijhmt

Effects of incidence angle on endwall convective transport within a high-turning turbine rotor passage

Sang Woo Lee *, Jin Jae Park

School of Mechanical Engineering, Kumoh National Institute of Technology, 1 Yangho-dong, Gumi, Gyeongbuk 730-701, Republic of Korea

ARTICLE INFO

Article history:
Received 8 August 2008
Received in revised form 7 January 2009
Accepted 1 July 2009
Available online 11 September 2009

Keywords:
Gas turbine
Off-design condition
Turbine rotor cascade
Incidence angle
Endwall heat transfer

ABSTRACT

Effects of incidence angle on the endwall convective transport within a high-turning turbine rotor passage have been investigated. Surface flow visualizations and heat/mass transfer measurements at off-design conditions are carried out at a fixed inlet Reynolds number of 2.78×10^5 for the incidence angles of $-10°$, $-5°$, 0, 5°, and 10°. The result shows that the incidence angle has considerable influences on the endwall local transport phenomena and on the behaviors of various endwall vortices. In the negative incidence case, convective transport is less influenced by the leading edge horseshoe vortex and by the suction-side corner vortex along their loci but is increased along the pressure-side corner vortex. In the case of positive incidence, however, convective transport is augmented remarkably along the leading edge horseshoe vortex, and is much influenced by the suction-side corner vortex. Moreover, heat/mass transfer is enhanced significantly along the pressure-side leading edge corner vortex. Local endwall convective transport in the area other than the endwall vortex sites is influenced significantly by the cascade inlet-to-exit velocity ratio which depends strongly on the incidence angle.

1. Introduction

For the advances in gas turbine performance, turbine durability due to hot gas temperature should be enhanced. Higher turbine inlet temperature generally causes increased metal temperature and steeper temperature gradients in the turbine hot components. Recent combustor design, which aims for reduced emissions, provides higher gas temperature near the turbine endwall with a flattened temperature distribution [1]. The turbine endwall thus needs a sophisticated cooling scheme as found in turbine blade cooling. For an efficient cooling configuration for the turbine endwall, it is essential to have a detailed description of heat transfer coefficient.

One of the earliest studies on the endwall heat transfer is presented by Blair [2], who conducted experiments to determine the film cooling effectiveness and heat transfer coefficient on a simulated turbine vane endwall with a cooling slot injection. Graziani et al. [3] measured local Stanton numbers on an electrically heated turbine endwall and blade surface for two different inlet boundary layer thicknesses. They found that the endwall heat transfer is affected strongly by the passage vortex, and the inlet boundary layer thickness on the endwall has a significant effect on the endwall and suction surface heat transfer. According to Gaugler and Russell [4], there is an obvious correlation between the visualized secondary flow and measured endwall Stanton number distribution near a vane cascade entrance, but the effects of the secondary flow are not obvious in the passage. York et al. [5] measured local Stanton numbers on a vane endwall with thermocouples for different Mach and Reynolds numbers. Employing the naphthalene sublimation technique, Goldstein and Spores [6] provided much detailed distributions of local endwall transport coefficient for a turbine rotor cascade. At a low turbulence level of about 1.2%, they investigated the effects of Reynolds number and inlet boundary layer thickness. Giel et al. [7] measured local endwall heat transfer coefficients for a transonic rotor cascade using a steady-state liquid crystal technique at low and elevated turbulence intensities of 0.25 and 7.0%. Kang et al. [8] and Kang and Thole [9] showed through endwall heat transfer measurements for a first-stage vane cascade that the peak heat transfer coefficient occurs coincidentally at the downward legs of both the horseshoe vortex and passage vortex. Radomsky and Thole [10] measured the endwall heat transfer under a combustor-level high turbulence intensity of 19.5% for the same vane cascade as Kang et al. [8] used. Their results show that the high turbulence enhances the endwall heat transfer, but the augmentation is either small or nonexistent in the leading edge region and near the suction-side of the blade. Lee et al. [11] studied effects of combustor-level high inlet turbulence on the endwall flow and heat transfer of a high-turning turbine rotor cascade. They successfully explained the endwall transport phenomena with flow visualization and heat/mass transfer data.

Gas turbines are sometimes at off-design conditions during their operation. At these off-design conditions, in general, incidence angle, *i*, may not be zero deg. Langston et al. [12] presented

---

* Corresponding author. Tel.: +82 54 478 7296; fax: +82 54 478 7319.
E-mail address: swlee@kumoh.ac.kr (S.W. Lee).

0017-9310/$ - see front matter © 2009 Elsevier Ltd. All rights reserved.
doi:10.1016/j.ijheatmasstransfer.2009.07.015

Nomenclature

b	axial chord length
c	chord length
c_p	constant-pressure specific heat
d	width of flow passage
D	diffusion coefficient of naphthalene in air
h	local heat transfer coefficient
h_m	local mass transfer coefficient
i	incidence angle ($\equiv (\beta_1 - \beta_1^0)$)
k	thermal conductivity
m	mass flow rate through a turbine
N	number of revolution of turbine rotor
p	pitch
P	pressure
Pr	Prandtl number ($\equiv(\mu c_p)/k$)
r	radial distance from turbine axis
Re_1	inlet Reynolds number ($\equiv(\rho W_{1\infty} c)/\mu$)
Re_2	exit Reynolds number ($\equiv(\rho W_{2\infty} c)/\mu$)
s	span
Sc	Schmidt number ($\equiv\mu/(\rho D)$)
St	local heat transfer Stanton number ($\equiv h/(\rho c_p W)$)
St_m	local mass transfer Stanton number ($\equiv h_m/W$)
St_{m1}	local mass transfer Stanton number based on$W_{1\infty}$ ($\equiv h_m/W_{1\infty}$)
St_{m2}	local mass transfer Stanton number based on $W_{2\infty}$ ($\equiv h_m/W_{1\infty}$)
T	temperature
Tu	turbulence intensity
U	rotational speed of turbine rotor blade ($\equiv r\omega$)
V	absolute velocity
V_a	axial velocity component of V
w	pitch-wise distance between the pressure and suction surfaces
W	relative velocity
$W_{1\infty}$	inlet free-stream relative velocity at the mid-span
$W_{2\infty}$	exit relative velocity at the mid-span ($\equiv(d_1/d_2)W_{1\infty}$)
x, y, z	cascade coordinates
y_p	pitch-wise (y-directional) coordinate from the suction surface

Greek symbols

α	angle of absolute velocity vector
β	angle of relative velocity vector
μ	absolute viscosity of air
ρ	density of air
ω	angular velocity ($\equiv 2\pi N$)

Subscripts

av	averaged over the whole measurement area
av,pch	averaged in the pitch-wise direction
0	total
1	turbine rotor blade inlet
2	turbine rotor blade exit
3	turbine inlet
4	turbine exit

Superscripts

0	zero incidence or design point
+	positive incidence
−	negative incidence

ink-trace flow visualizations on the endwall of a turbine cascade for two incidences of zero and +11.8°. They showed that the saddle point on the inlet endwall moves to the suction-side as the incidence angle increases. Hodson and Dominy [13] investigated internal flow mechanisms of a high-speed linear cascade under various off-design conditions and found that low-momentum endwall fluid migrates more intensely onto the blade suction surface as the incidence angle increases. Yamamoto [14] studied interaction mechanisms between the tip-leakage flow and the passage vortex in a linear turbine cascade with tip clearance gap at off-design conditions. Yamamoto and Nouse [15] investigated the effects of incidence on cascade three-dimensional flows near the endwall of a turbine rotor cascade and the associated loss mechanisms. Yamamoto [16] measured three-dimensional flow and loss data within a linear turbine cascade passage with tip clearance, and also reported the detailed three-dimensional flows within the tip clearance gap and interactions of the tip-leakage flow with the main passage flow. Jouini et al. [17] presented detailed measurements of the mid-span aerodynamic performance of a transonic turbine cascade at off-design conditions. Profile losses were reported for incidence angles of −10°, 0°, 4.5°, 10°, and 14.5°. Brear et al. [18] investigated pressure surface separations at the mid-span of a low-pressure turbine cascade for three incidence angles of −10°, 0°, and 10°. Recently, Rhee and Cho [19,20] reported heat/mass transfer characteristics not only on a near-tip surface [19] but also tip surface and shroud [20] in a low-speed annular cascade for the incidence angles of −15° to 7°.

The previous studies on the turbine endwall heat transfer were conducted only at their design points, and the above-mentioned investigations at off-design conditions were mainly focused on flow phenomena and aerodynamic loss generations, except for the heat/mass transfer measurements on the near-tip blade surface and tip/shroud surface by Rhee and Cho [19,20]. As far as the authors know, there seem to be no heat transfer data on the endwall reported at off-design conditions. In this study, incidence angle effects on the endwall convective transport within a high-turning turbine rotor blade passage have been investigated by using the naphthalene sublimation technique.

2. Velocity triangles at off-design conditions

A turbine is operated at the design point, when it is running at the particular blade rotational speed, pressure ratio, and mass flow rate for which it is designed. However, any turbine is required to operate at conditions far removed from the design point including engine starting, idling, reduced power, increased power, acceleration, and deceleration. Thus it is clear that turbines must be capable of satisfactory operation at off-design conditions over a wide operation range.

Fig. 1 shows typical off-design turbine mass flow characteristics from Cohen et al. [21]. $mT_{03}^{0.5}/P_{03}$ relative to the design point value is plotted against pressure ratio P_{03}/P_{04} with the variation of $N/T_{03}^{0.5}$ relative to the design point value. m and N indicate mass flow rate through the turbine and number of revolution in turn. T_{03} is total temperature at the turbine inlet, and P_{03} and P_{04} are total pressures at the turbine inlet and exit, respectively. At a pressure ratio which produces choking conditions at the turbine nozzle throats, $mT_{03}^{0.5}/P_{03}$ relative to the design point value reaches a maximum value of about unity and the constant $N/T_{03}^{0.5}$ lines merge into a single

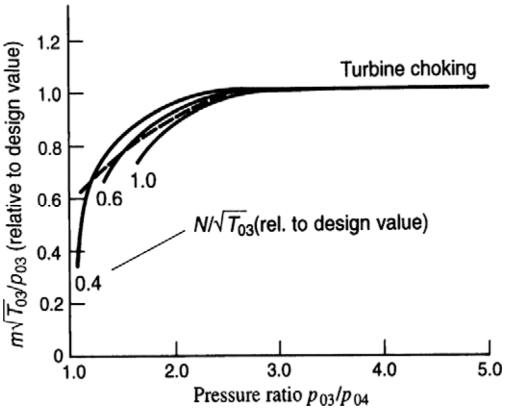

Fig. 1. Typical off-design turbine mass flow characteristics [21].

horizontal one. If choking occurs in the rotor blade passage or outlet annulus, the maximum value of $mT_{03}^{0.5}/P_{03}$ varies slightly with $N/T_{03}^{0.5}$ as in [22]. Choking at the nozzle throats is a more normal situation.

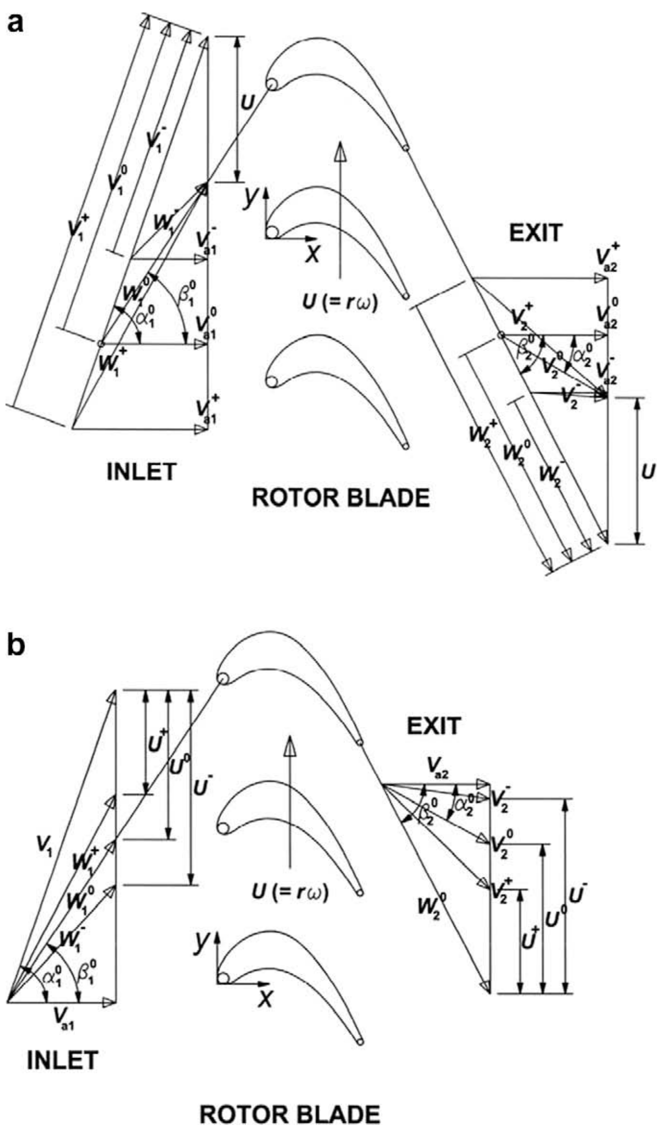

Fig. 2. Velocity triangles at off-design conditions. (a) Variable axial velocities at a fixed rotation speed; (b) variable rotating speeds at a fixed axial velocity.

It is very important to understand how the rotational speed and mass flow rate alter velocity triangles at the inlet and exit of a rotor blade passage at off-design conditions. The velocity triangles for two simple operating conditions of a fixed rotational speed (U = constant) and a fixed axial velocity (V_a = constant) are presented in Fig. 2. Velocities V and W in Fig. 2 are absolute and relative velocities, respectively. The superscripts of "–", "0", and "+" indicate negative, zero, and positive incidences, respectively, and the subscripts of "1" and "2" mean the inlet and exit of the blade passage in turn. The incidence angle, i, is defined as $(\beta_1 - \beta_1^0)$. Fig. 2a shows typical mid-span velocity triangles with different axial velocities at a fixed rotational speed of U. In this case, an axial velocity higher than the design point one, the velocity V_{a1}^+ results in a positive incidence angle, meanwhile V_{a1}^-, which is lower than the design point, leads to a negative incidence angle. Both of the inlet and exit relative velocities increase in the positive incidence case but decrease in the negative incidence case, in comparison with the corresponding design point values. Fig. 2b shows typical mid-span velocity triangles with different rotational speeds at a fixed axial velocity. In this case, a rotational speed higher than the design point, U^-, results in a negative incidence angle, meanwhile U^+, which is lower than U^0, leads to a positive one. Inlet relative velocity increases at the positive incidence angle but decreases at the negative one, compared to the design point value, meanwhile exit relative velocity remains unchanged for all incidence angles.

Mass flow rate and rotational speed in actual turbines which have typical off-design characteristics, as in Fig. 1, would be lower than the design point ones, respectively, because $mT_{03}^{0.5}/P_{03}$ and $N/T_{03}^{0.5}$ relative to the corresponding design point values are lower than unity. A lower axial velocity from the lower mass flow rate leads to a negative incidence angle, lower inlet relative velocity, and lower exit relative velocity, as shown in Fig. 2a. On the other hand, the lower rotational speed delivers a positive incidence angle, higher inlet relative velocity, but no change in exit relative velocity, as shown in Fig. 2b. From the above discussions, it is noted that negative incidences arise mainly from lower turbine mass flow rates but positive incidences are usually attributed to lower rotational speeds, in comparison with the design point values.

Fig. 3 shows the relation between the inlet and exit relative velocities at the mid-span of the present turbine rotor blade with the variation of i. In this impulse/reaction turbine rotor blade passage, energy of the on-coming gas flow is absorbed on its impact with the blade and during the subsequent reaction through the blade passage to rotate the turbine shaft. Relative velocity tends to increase through the convergent passage during the reaction process. Therefore, W_1/W_2 is lower than unity even at the design point of i = 0°. In the case of negative incidence, W_1/W_2 tends to decrease as the absolute value of i increases. On the other hand, W_1/W_2 tends to increase with increasing i in the case of positive

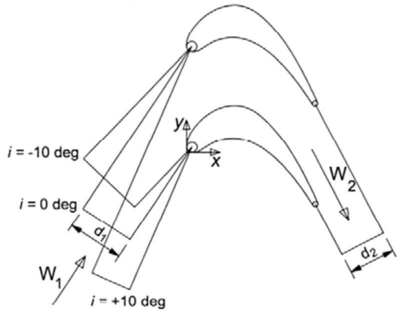

$$W_1 = \frac{d_2}{d_1} W_2$$

i (deg)	$\frac{W_1}{W_2}$
-10.0	0.667
-5.0	0.738
0.0	0.832
+5.0	0.961
(+6.2)	(1.000)
+10.0	1.150

Fig. 3. Inlet-to-exit velocity ratio at mid-span.

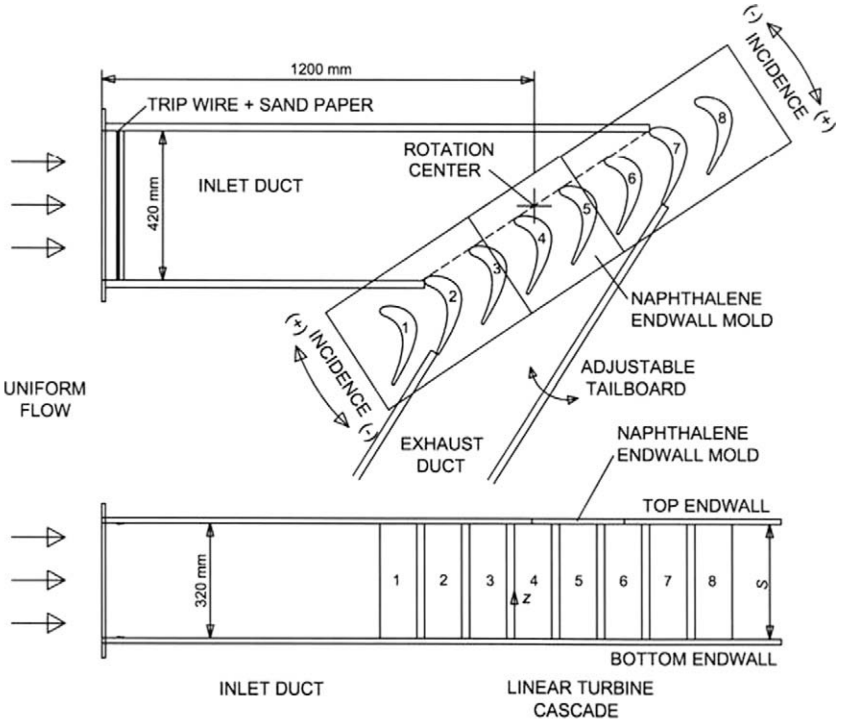

Fig. 4. Overall view of cascade wind tunnel.

incidence. There would be no reaction within the turbine blade passage, especially when $i > 6.2°$, because W_1/W_2 is not lower than unity any more.

3. Experimental apparatus and procedure

3.1. Linear cascade wind tunnel

As shown in Fig. 4, the cascade wind tunnel comprises an open-circuit type wind tunnel, an inlet duct, a linear turbine cascade, and an exhaust section. The inlet duct has a cross section of 0.42 m × 0.32 m. The flow coming out from the wind tunnel is developing to a turbulent boundary layer flow on the top and bottom walls of the inlet duct, after passing a trip wire and sand paper. In this study, five different inlet ducts are prepared for the incidence angles of $i = -10°, -5°, 0°, 5°$, and $10°$. At each i, the turbine cascade and the exhaust duct are rotated in one with respect to the rotation center as indicated in Fig. 4. Therefore, its central entrance can be located about 1.20 m downstream of the wind tunnel exit regardless of i. As can be seen in Fig. 4, clock-wise rotation delivers positive incidence. The linear turbine cascade has eight blades, but the number of blades actually used depends on i. The exhaust duct has a tailboard to adjust periodicity among the blade passage flow.

The blades are fabricated based on the mid-span profile of a high-pressure first-stage turbine rotor blade for power generation. The rotor blade profile used in this study is presented in Lee and Chae [23]. In the xyz coordinates, x, y, and z are in the axial, pitch-wise and span-wise directions of the cascade. As listed in Fig. 5, the chord length, c, axial chord, b, pitch, p, and span, s, are 217.8 mm, 196.0 mm, 151.6 mm, and 320.0 mm, respectively. The span is determined based on an aspect ratio of the original rotor blade. The blade turning angle is given as 119°. Static pressures around the blade are measured at 22 pressure-sensing holes located along the blade #4 and those obtained at $i = 0$ deg are reported in Lee and Chae [23].

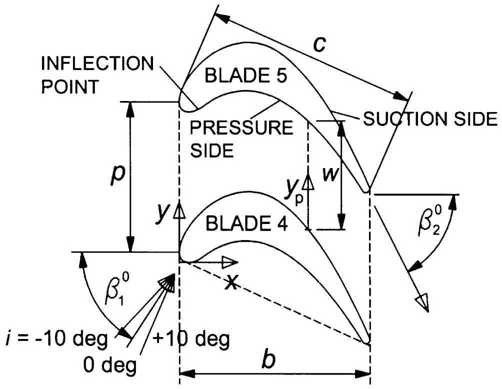

Number of blades	6
Chord length (c)	217.8 mm
Axial chord (b)	196.0 mm
Pitch (p)	151.6 mm
Span (s)	320.0 mm
Blade inlet angle (β_1^0)	56.4 deg
Blade outlet angle (β_2^0)	-62.6 deg

Fig. 5. Arrangement of turbine blade cascade.

3.2. Surface flow visualizations

For the precise identification of an endwall separation line, we employed an oil film method using a mixture of carbon black and kerosene. In this study, only the upstream region 120 mm ahead of the leading edges is initially coated with the oil film mixture in the same way employed by Lee et al. [24], instead of its full coverage. In order to make the mixture move easily with near-wall flow, kerosene was spread on the whole area of the endwall surface before the upstream partial coating with the mixture. These surface flow visualizations are conducted on the bottom endwall of the turbine passage.

3.3. Naphthalene sublimation technique

In the present experiments, local mass transfer coefficient, h_m, is measured by employing the naphthalene sublimation technique. h_m can be evaluated from the corresponding local sublimation depth of cast naphthalene. Mass transfer Stanton number, St_m, is commonly used as a dimensionless mass transfer coefficient.

Heat transfer Stanton number, St, can be obtained according to an analogy between heat and mass transfer [25] of

$$\frac{St}{St_m} = \left(\frac{Pr}{Sc}\right)^{n-1}. \tag{1}$$

The constant n is usually taken to be 1/3 for a laminar flow and to be 0.4 for a turbulent flow [25,26]. The magnitude of Pr for air is about 0.7, and the value of Sc for naphthalene diffusion into air is approximately 2.28 depending slightly on temperature [26]. The boundary condition in the mass transfer system is equivalent to the constant surface temperature condition in the heat transfer system.

In this study, mass transfer Stanton number based on the inlet free-stream relative velocity of $W_{1\infty}$ is defined as

$$St_{m1} = \frac{h_m}{W_{1\infty}}. \tag{2}$$

Mass transfer Stanton number can also be defined based on $W_{2\infty}$ in the following way:

$$St_{m2} = \frac{h_m}{W_{2\infty}}. \tag{3}$$

The mid-span exit relative velocity, $W_{2\infty}$, is defined as follows:

$$W_{2\infty} = \left(\frac{d_1}{d_2}\right)W_{1\infty}. \tag{4}$$

3.4. Naphthalene coated endwall

An endwall mold for naphthalene casting is shown in Fig. 6. The endwall mold and its well-polished cover are made of aluminum. A layer of naphthalene is cast inside the grooved cavity between them and has a thickness of 8 mm. The cast endwall is installed on the top of the turbine cascade as in Fig. 4. A T-type thermocouple is embedded in the cast naphthalene to measure naphthalene surface temperature. Sublimed depth is measured at 50 points in the *x*-direction and at 21 points in the *y*-direction as can be seen in Fig. 6. Considering the presence of a fillet along the original blade-endwall corner, the measurement locations adjacent to the corner line are kept about 2 mm apart from it.

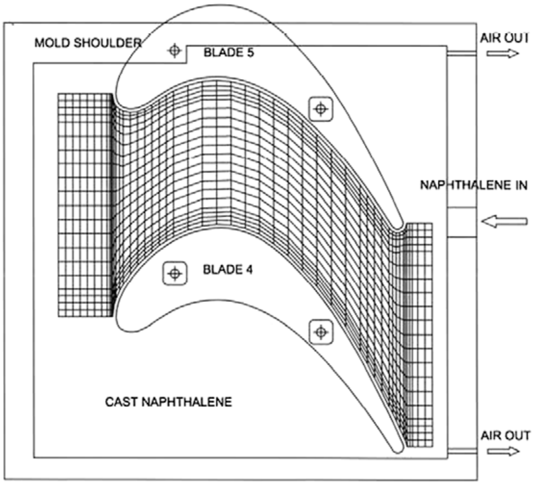

Fig. 6. Naphthalene mold and sublimation depth measurement locations.

3.5. Data reduction systems

Measurements of pressure, temperature and naphthalene sublimation depth are controlled by a personal computer equipped with plug-in boards such as a Multi-Function DI/O Board (National Instruments, PCI-MIO-16E-4) and a GPIB adapter (National Instruments, AT-GPIB). Measured pressures are transformed into DC voltages by a digital micro monometer (MKS, 223BD-00010ACB), and these signals are sampled by a 12-bit A-D converter in the Multi-Function DI/O Board, and then transferred to the computer. Temperatures of the inlet free-stream air and the cast naphthalene are measured with T-type thermocouples connected to a digital voltmeter (Keithley, Model 2001TSCAN), which is controlled by the computer through the GPIB. The thermocouples are calibrated using a constant-temperature bath (Fisher Scientific, 9010) and a standard thermometer. Temperature measurements are based on STP 470A [27] published by ASTM.

A LVDT (linear variable differential transformer) depth gauge (Sensortec, 060-3590-02) is used to measure local sublimation depth. Its full scale and resolution are ±0.5 mm and 0.5 μm, respectively. In actual exposure experiments, average sublimation depth is maintained approximately at about 0.1 mm, and maximum sublimation depth is less than about 0.3 mm. When a smooth solid surface of naphthalene is obtained from the cast procedure, the cast endwall is placed on a two-axis positioning system, which is equipped with linear motion guides (Samik, SAR1615T), stepping motors (Oriental Motor, UPH599-A), and stepping motor drivers (Oriental Motor, UDX5114). The first scanning of the naphthalene surface is conducted with the calibrated depth gauge at 1050 locations, before exposure to the air flow. It takes about 25 min to complete the total scanning. The readings of local elevation are recorded in the computer through the 12-bit A-D converter. Then, the cast endwall is positioned in the cascade. After it is exposed to the air flow for about 90 min, it is brought back to the positioning system, and is scanned again. The difference between the before-and-after readings at each location still includes free-convection loss during the setup time of the cast endwall as well as during the depth measurements. The net sublimation depth is finally obtained after the subtraction of the free-convection loss.

4. Operating conditions and uncertainties

At off-design conditions, incidence angle is considered a key parameter to characterize flow phenomena within blade passages. In actual turbine operations as discussed earlier, it should be noted that in comparison with the design point values, negative incidence resulted from lower turbine mass flow rate leads not only to lower inlet relative velocity but also to lower exit one, meanwhile positive incidence arising from lower rotational speed delivers higher inlet relative velocity but the same exit one. Therefore, it would be inevitable to have a Reynolds number effect, if either a fixed inlet or a fixed exit velocity condition is employed in the investigation of incidence effects.

In this study, endwall surface flow visualizations are conducted for $i = -10°$ and $10°$. On the other hand, mass transfer experiments are performed at five incidence angles of $i = -10°$, $-5°$, $0°$, $5°$ and $10°$. During the present experiments, inlet free-stream relative velocity and turbulence intensity are maintained as $W_1 = 20.0$ m/s and $Tu = 1.2\%$ $1.5c$ upstream of the cascade entrance. As summarized in Table 1, the inlet Reynolds number based on W_1 and c, is fixed as

Table 1
Experimental conditions.

i (°)	$W_{1\infty}$ (m/s)	Re_1	$W_{2\infty}$ (m/s)	Re_2
−10	20.0	2.78×10^5	30.0	4.17×10^5
−5			27.1	3.77×10^5
0			24.0	3.34×10^5
5			20.8	2.89×10^5
10			17.4	2.42×10^5

$\mathrm{Re}_1 = 2.78 \times 10^5$ but the exit Reynolds number based on W_2 and c, Re_2, as well as W_2 has different values depending on i. The exit Reynolds number deviation is within about 30% of the design point value of Re_2. At the location 1.5c upstream of the cascade entrance, the boundary layer thickness, displacement thickness, and momentum thickness are 44.7 mm, 5.16 mm, and 4.04 mm, respectively. These values are equivalent to 14.0%, 1.6%, and 1.3% of the span, and 20.5%, 2.4%, and 1.9% of the chord length, in turn. The thicknesses are kept constant independent of i due to the fixed value of W_1 in this study. Good pitch-wise mean flow periodicities are obtained at the entrance of the central three blade passages within 2% deviation for the tested incidence angles. During each sublimation experiment, naphthalene surface temperature is maintained within 0.2 °C.

The uncertainty interval of mass transfer Stanton number with 95% confidence based on Abernethy et al. [28] is estimated to be ±5.7% of St_{m1}. Mass transfer data at $i = 0°$ in this study is compared with that in the low turbulence case ($Tu = 1.2\%$) of Lee et al. [11], which was conducted at the same operating conditions and in the same facility as the present ones. This repeatability test shows that the difference in $(\mathrm{St}_{m1})_{av}$ falls within 2.96%.

5. Results and discussion

5.1. Local heat/mass transfer rate at the design point

The baseline distribution of St_{m1} at $i = 0°$ measured by Lee et al. [11] is presented in Fig. 7. The following discussions at the design point are based on Lee et al. [11]. Three-dimensional vortex flows developing over the endwall within a turbine rotor passage at $i = 0°$ are presented schematically by Goldstein and Spores [6]. The entire endwall surface can be classified into seven different regions from Region A to Region G. Relatively low St_{m1} is found in Region A at the entrance of the cascade because incoming boundary layer still extends in this area without any disturbances by the blades. Downstream of the separation line A^0–B^0 in Fig. 7, there is a higher heat/mass transfer rate region near the leading edge, Region B, which has pressure- and suction-side wings indicated by the long and short arrows, respectively. The long pressure-side wing extends from the attachment line almost up to the suction-side of the neighboring blade across the flow passage nearly in parallel with the separation line. The long arrow is equivalent to the locus of a pressure-side leg of the leading edge horseshoe vortex. This pressure-side leg develops into a passage vortex after crossing the flow passage. Contrary to the pressure-side wing, the suction-side wing has a very small area on the opposite side and is resulted from a suction-side leg of the leading edge horseshoe vortex. A maximum value of St_{m1} occurs along the corner line of the leading edge. This severe thermal load is attributed to the existence of a pair of leading edge corner vortices. Region C is situated near the area where the incoming boundary layer flow without separation meets the suction surface. The near-wall flow rushing toward the suction surface in the region upstream of the neighboring separation lines interacts strongly with it in Region C, resulting in a considerable flow disturbance. Consequently, the local mass transfer in Region C is fairly enhanced. There exists a pressure-side corner vortex along the corner line between the endwall and the pressure surface. Higher St_{m1} observed in Region D is resulted from the presence of a pressure-side corner vortex. Region E is in the form of a long strip along the suction-side corner. In Region E, there is a very steep gradient as well as a relatively high value of St_{m1}, due to the presence of a suction-side corner vortex. This region is equivalent mostly to the area bounded by the line A^0–C^0. Fig. 7 also shows that the suction-side corner vortex provides higher heat/mass transfer rate with a broader residing area than the pressure-side one. All over the endwall surface, the lowest heat/mass transfer rate is found in Region F. The value of St_{m1} in Region F is as low as about 1.0×10^{-3}, which is about one fifth of the highest value of St_{m1} in Region B. Severe thermal load is also found in Region G just behind the trailing edge. In this wake region, there exists an unsteady periodic vortex shedding. These endwall transport phenomena at $i = 0°$ are also discussed by Goldstein and Spores [6] in detail.

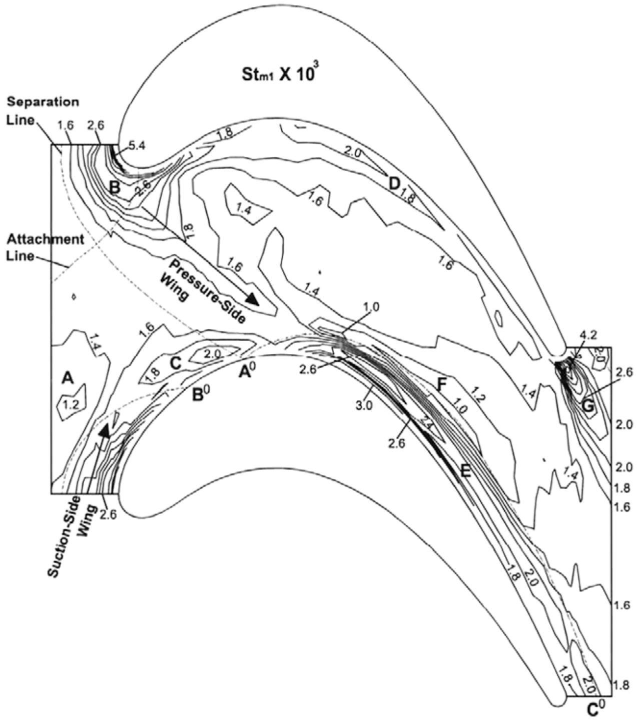

Fig. 7. Contours of St_{m1} at $i = 0°$ from Lee et al. [11].

5.2. Surface flow visualization at off-design conditions

Endwall flow visualizations at $i = -10°$ and 10° are presented in Fig. 8a and b. The superscripts of "−" and "+" in Fig. 8 denote the cases of $i = -10°$ and 10°, respectively. The visualizations clearly show three-dimensional flow separation of the incoming boundary layer flow. The line connecting the downstream bound of oil film traces line A–B is considered as a separation line. There exists no oil film mixture in the region downstream of the separation line, because oil film cannot lift off the endwall with separated fluid due to the gravity. The mixture approaching the cascade passage turns toward the suction surface in the region upstream of the adjacent separation lines, and then collides with it between the points A and B. Finally, the mixture climbs onto the suction surface, overcoming gravity. Some of the mixture moves downstream on the suction surface with an aid of up-wash momentum of the passage vortex, while the remainder near the root of the blade is entrained into an endwall area surrounded by the line A–C. The mixture moving downstream on the suction surface is separated from it at the trailing edge, and then touches the endwall again. These endwall flow phenomena are observed regardless of i, but

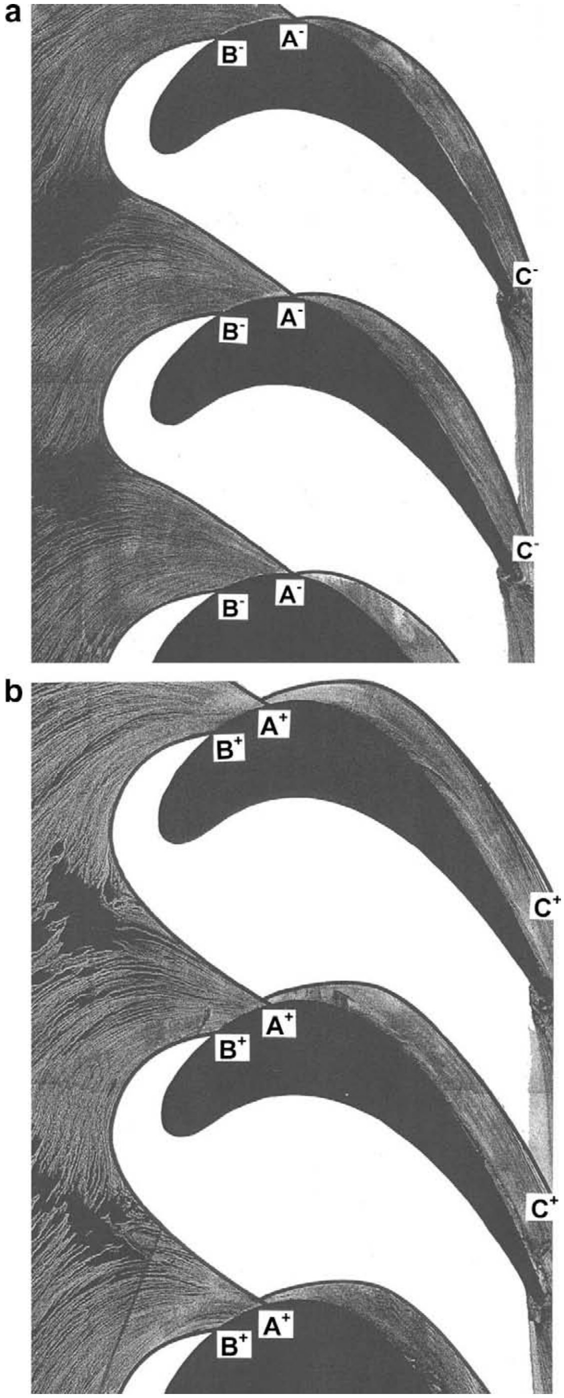

Fig. 8. Endwall surface flow visualizations. (a) $i = -10°$; (b) $i = 10°$.

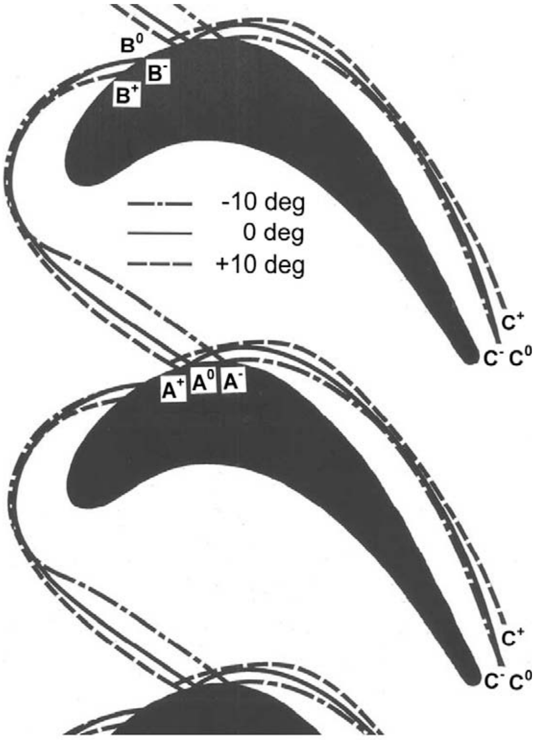

(Flow boundaries at i = 0 deg from [11])

Fig. 9. Comparison of endwall flow boundaries.

there exist some differences in the flow boundaries between the two cases.

In Fig. 9, the endwall flow boundaries at $i = -10°$ and 10° in Fig. 8 are compared directly with that at $i = 0°$ in Lee et al. [11] for $Tu = 1.2\%$ and $R_1 = 2.78 \times 10^5$. This comparison shows that the flow boundaries at $i = 0°$ are located between those at $i = -10°$ and 10°. Comparing the two cases of $i = -10°$ and 10°, there is a large discrepancy in the lower half of the separation line near the point A^0, but a slight difference is observed in the upper half of it.

Compared to the zero incidence case, there is a considerable advancement of the lower portion of the separation line near the point A^- at $i = -10°$. This is because there is a weaker flow blockage by the turbine blades at the cascade entrance than that at $i = 0°$, due to the wider inlet flow passage and lower turning of flow as shown in Fig. 3. This weaker flow blockage would lead to a suppressed leading edge horseshoe vortex and then to a weaker passage vortex in turn. Fig. 9 shows also that the area surrounded by the line A^-–C^- and the suction-side boundary at $i = -10°$ is narrowest. This means that the suction-side corner vortex developing underneath the weaker passage vortex tends to be weakened. The advancement of the separation line delivers more oblique collision of the un-separated incoming near-wall flow with the suction surface in the area between the two adjacent points of A^- and B^- in Fig. 8a, which could reduce flow instability along the suction-side corner line. This is one of the reasons why the suction-side corner vortex is weakened at $i = -10°$.

On the other hand, there is not only a retreat of the lower portion of the separation line near the point A^+ but also an advancement of its upper portion near the point B^+ at $i = 10°$, although their amounts are much smaller than those of the advancement at $i = -10°$. This fact implies that incoming flow faces stronger blockage than that at $i = 0°$, due to the narrower inlet flow passage and higher turning of flow, as shown in Fig. 3. As a result, the leading edge horseshoe vortex at $i = 10°$ would be reinforced and the passage vortex is amplified. The area surrounded by the line A^+–C^+ is wider, in comparison with the zero and negative incidence cases, which suggests that the suction-side corner vortex in this positive incidence case is strengthened. Due to the change in the separation line at $i = 10°$, un-separated incoming near-wall flow collides with the suction surface more normally between the neighboring points of A^+ and B^+ in Fig. 8b, which could make the suction-side corner flow more unstable and stimulate the vortex development.

5.3. Local heat/mass transfer rates at off-design conditions

Fig. 10 shows contours of St_{m1} at off-design conditions. Even at the negative incidence of $i = -10°$ (Fig. 10a), the endwall area can

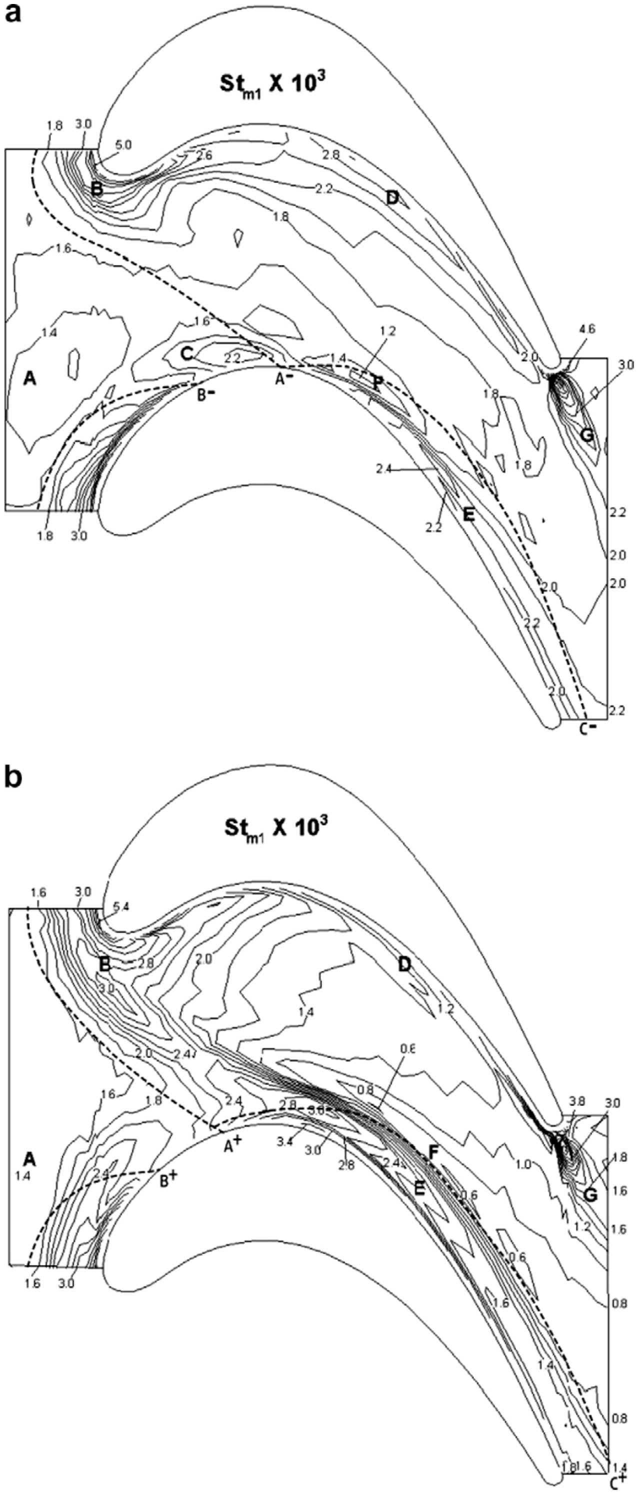

Fig. 10. Contours of $\mathrm{St}_{\mathrm{m1}}$. (a) $i = -10°$; (b) $i = 10°$.

be classified into the seven distinct regions. However, there are somewhat different heat/mass transfer characteristics in comparison with those at $i = 0°$. The most noticeable difference is observed in Region B and in Region E. The clear locus along the pressure-side wing in Fig. 7 cannot be identified in Fig. 10a. Region E in Fig. 10a has fairly low $\mathrm{St}_{\mathrm{m1}}$, and it also has a narrower occupation area in comparison with that at $i = 0°$. These tendencies imply that the negative incidence weakens the leading edge horseshoe vortex and the following passage vortex in turn, and suppresses the suction-side corner vortex underneath the weakened passage vortex. This theory can also be supported by the considerable advancement of the separation line near the point A^- and by the narrowest area surrounded by the line A^-–C^- in Fig. 9. The local mass transfer in Region F is also influenced by this negative incidence. $\mathrm{St}_{\mathrm{m1}}$ in Region F has higher values and its area is reduced, compared with those in Fig. 7. Local heat/mass transfer rate in Region D in Fig. 10a is much enhanced, which means that the negative incidence intensifies the pressure-side corner vortex, due to the flow destabilization downstream of the inflection point shown in Fig. 5. On the other hand, there are no considerable changes in $\mathrm{St}_{\mathrm{m1}}$ in Region A, Region C, and Region G. A close examination in the downstream region from the mid-chord to the trailing edge shows that the central passage area other than the seven regions at $i = -10°$ has higher $\mathrm{St}_{\mathrm{m1}}$, compared with that at $i = 0°$. This is because W_2 at $i = -10°$ is higher than that at $i = 0°$ in the case of a fixed value of W_1, as shown in Table 1. At $i = -5°$, heat/mass transfer characteristics provide the same qualitative tendencies as those at $i = -10°$, but various near-wall flow phenomena arising from negative incidence are found less severe than those at $i = -10°$.

Fig. 10b shows contours of $\mathrm{St}_{\mathrm{m1}}$ at $i = 10°$. At this positive incidence angle, there are significant changes in the $\mathrm{St}_{\mathrm{m1}}$ distribution, particularly at the entrance of the cascade and along the suction-side corner line. The remarkable augmentation of $\mathrm{St}_{\mathrm{m1}}$ in the region farther upstream of the leading edge in comparisons with the cases of $i = -10°$ and 0° demonstrates that the leading edge horseshoe vortex is much intensified due to the strong blockage of the incoming near-wall flow, as discussed earlier in the flow visualizations. The trajectories of its pressure- and suction-side legs at $i = 10°$ are most noticeable among the three cases. Moreover, the locus of the pressure-side leading edge corner vortex can be clearly identified around the leading edge slightly away from it at $i = 10°$. This higher $\mathrm{St}_{\mathrm{m1}}$ area near the leading edge extends far downstream along the pressure-side corner line up to the mid-chord. On the other hand, there seems to be no big change in the suction-side leading edge corner vortex. This is in contrast with the strong intensification of a suction-side leg of the leading edge horseshoe vortex. Region C, which can be seen clearly in Figs. 7 and 10a, is not existent in Fig. 10b, because this region at $i = 10°$ appears to be influenced directly not only by the intensified suction-side leg of the horseshoe vortex but also by the intensified adjacent pressure-side leg of it. Due to the extension of the pressure-side leading edge corner vortex up to the mid-chord, it is not easy to identify the pressure-side corner vortex in Region D from it at $i = 10°$. However, it is clear that $\mathrm{St}_{\mathrm{m1}}$ in Region D in this case is much lower than that at $i = -10°$. There exists a strong suction-side corner vortex underneath the intensified passage vortex resulted from the reinforced pressure-side leg of the leading edge horseshoe vortex. Therefore, Region E in Fig. 10b has the broadest area with the highest $\mathrm{St}_{\mathrm{m1}}$ among the three cases. This is consistent with the fact that the area surrounded by the line A^+–C^+ is widest as in Fig. 9. The reinforced pressure-side leg provides the lowest value of $\mathrm{St}_{\mathrm{m1}}$ in Region F and the widest area of it. There is no big change in $\mathrm{St}_{\mathrm{m1}}$ in Region G for the three incidences. This suggests that the vortex shedding behind the trailing edge is not much influenced by the change in i. The distribution of $\mathrm{St}_{\mathrm{m1}}$ in the region from the mid-chord to the trailing edge in Fig. 10b shows that the central passage area outside the seven regions has lower $\mathrm{St}_{\mathrm{m1}}$ compared with that at $i = 0°$, because W_1 at $i = 10°$ is lower than that at $i = 0°$ as in Table 1 under the present fixed inlet velocity condition. Heat/mass transfer characteristics at $i = 5°$ also deliver the same qualitative trends as that in the case of $i = 10°$.

Distributions of $\mathrm{St}_{\mathrm{m1}}$ along the centerline of flow passage of $y_p/w = 0.5$ are shown in Fig. 11. In the region upstream of the cascade entrance ($x/b < 0.0$), the incidence effect on $\mathrm{St}_{\mathrm{m1}}$ is negligibly small, because $\mathrm{St}_{\mathrm{m1}}$ is based on the fixed inlet free-stream velocity

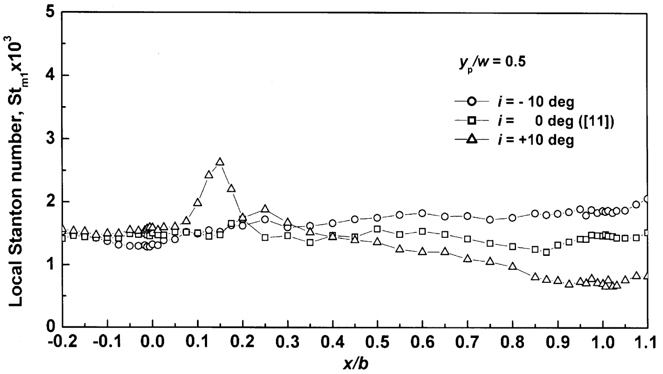

Fig. 11. Profiles of St_{m1} along the flow passage centerline of $y_p/w = 0.5$.

of $W_{1\infty} = 20$ m/s. As moving downstream, however, the incidence effect becomes considerable. In the downstream region of $x/b > 0.5$, in general, the negative incidence results in higher St_{m1} but the positive incidence results in lower St_{m1}, in comparison with that at $i = 0°$. Particularly at the exit of the cascade ($x/b = 1.0$), St_{m1} at $i = -10°$ is about three times higher than that at $i = 10°$. This is mainly because as i increases from $-10°$ to $10°$, $W_{2\infty}$ decreases from 30.0 to 17.2 m/s as in Table 1. In addition, more incoming near-wall fluid is fed to form the leading edge horseshoe vortex at $i = 10°$, due to the intensification of it. As a result, the reduced mass flow rate near the endwall leads to lower convective transport in the downstream region. On the other hand, the weakened leading edge horseshoe vortex at $i = -10°$ can contribute to the enhancement of the downstream convective transport. At $i = 0°$, there exist a small local peak of St_{m1} at $x/b = 0.2$. A tiny local peak of St_{m1} is barely found at $x/b = 0.25$ at $i = -10°$, meanwhile there is a huge local peak of St_{m1} at $x/b = 0.15$ at $i = 10°$. These peaks are resulted from the pressure-side leg of the leading edge horseshoe vortex, and the peak value is proportional to its strength. Among the three cases, the peak at $i = 10°$ has the highest value of St_{m1} and is located most upstream.

Pitch-wise variations of St_{m1} at $x/b = 0.75$ are presented in Fig. 12. This shows that St_{m1} in the central passage area has an increasing tendency in the positive y_p-direction regardless of i. When y_p/w is larger than 0.3, St_{m1} decreases noticeably with the increment of i from $-10°$ to $10°$. The region occupied by the suction-side corner vortex, Region E, is much wider than that by the pressure-side one, Region D. As the incidence angle increases from $-10°$ to $10°$, the local minimum value of St_{m1} in Region F decreases noticeably and its location shifts far away from the suction-side.

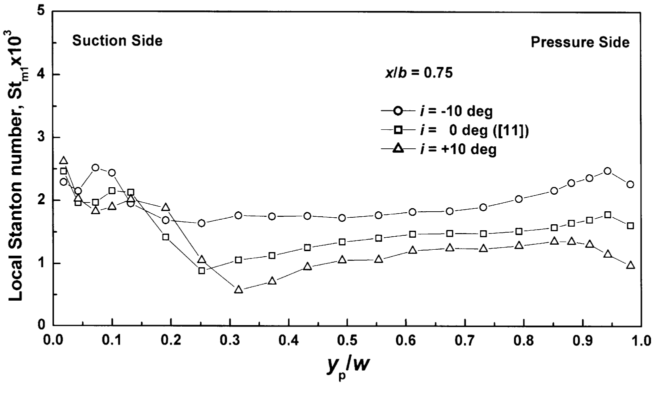

Fig. 12. Profiles of St_{m1} in the pitch-wise direction at $x/b = 0.75$.

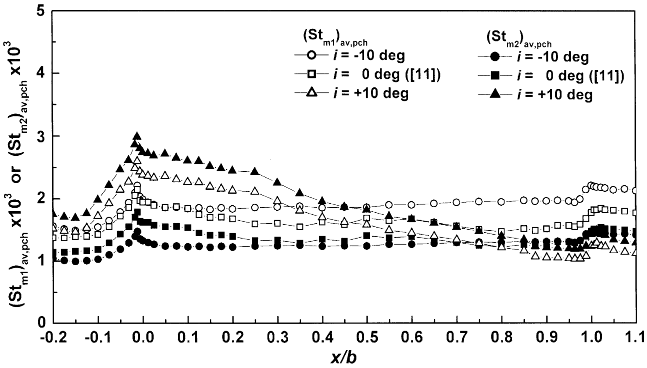

Fig. 13. Profiles of $(St_{m1})_{av,pch}$ and $(St_{m2})_{av,pch}$.

5.4. Average heat/mass transfer rates at off-design conditions

Mass transfer rates averaged in the pitch-wise or in the y-direction are introduced in Fig. 13. In this figure, pitch-wise averaged mass transfer coefficients are reported not only in the form of $(St_{m1})_{av,pch}$ based on $W_{1\infty}$ but also in the form of $(St_{m2})_{av,pch}$ based on $W_{2\infty}$ as in Eqs. (2) and (3). Inlet flow conditions are identical regardless of i, because $W_{1\infty}$ has a fixed value of 20 m/s throughout the experiments. Therefore, $(St_{m1})_{av,pch}$ in the upstream region of the cascade has nearly the same value regardless of i. $(St_{m1})_{av,pch}$ increases steeply as approaching the cascade entrance and has a sharp peak at $x/b = 0.0$. At $x/b = 1.0$, there is another local maximum of $(St_{m1})_{av,pch}$. In the region where $x/b < 0.3$, $(St_{m1})_{av,pch}$ at $i = 10°$ is found highest. In the region where $x/b > 0.5$, $(St_{m1})_{av,pch}$ has lower values at $i = 10°$ but has higher value at $i = -10°$ than that at $i = 0°$. Considerable discrepancies of $(St_{m1})_{av,pch}$ among the three cases in the downstream region are resulted from the different values of $W_{2\infty}$ as listed in Table 1.

On the contrary, $(St_{m2})_{av,pch}$ in the upstream region shows remarkable discrepancies among the three cases. If off-design experiments were conducted at a fixed exit velocity of $W_{2\infty}$, there would be a wide spread of $(St_{m2})_{av,pch}$ in the upstream region as in Fig. 13, due to the changes in convective transport arising from different inlet velocities. In the region where $x/b < 0.8$, $(St_{m2})_{av,pch}$ at $i = 10°$ is found much higher than the others, due to the intensified leading edge horseshoe vortex as well as a lower value of $W_{2\infty}$. In the downstream region, discrepancies of $(St_{m2})_{av,pch}$ among the three cases are found very small in spite of the different exit

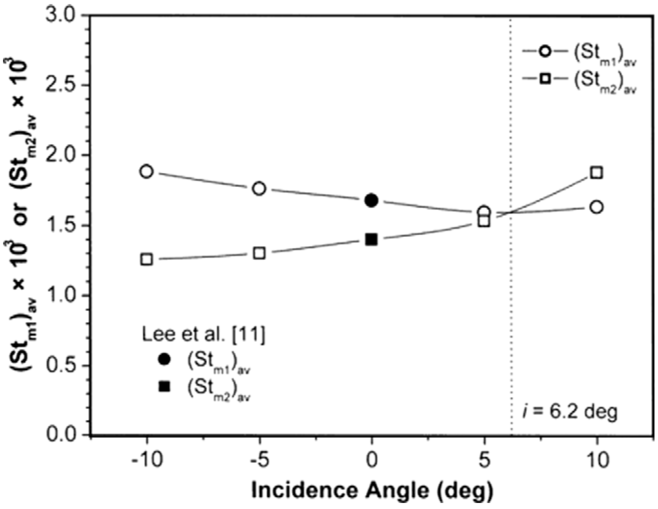

Fig. 14. $(St_{m1})_{av}$ and $(St_{m2})_{av}$ as a function of i.

Reynolds numbers. This fact implies that for the incidence angles and Reynolds numbers tested in this study, Reynolds number has only a minor effect on the endwall convective transport in comparison with the incidence angle effect.

Mass transfer Stanton number averaged across the whole measurement area is reported in the forms of $(St_{m1})_{av}$ and $(St_{m2})_{av}$ in Fig. 14 as a function of *i*. $(St_{m1})_{av}$ has a tendency to decrease mildly with increasing *i* from $-10°$ to 5°. With respect to that at $i = 0°$, $(St_{m1})_{av}$ is augmented by 15.4% at $i = -10°$ and is almost unchanged at $i = 10°$. With the increment of *i* from −10 to 10°, $(St_{m2})_{av}$ based on $W_{2\infty}$ tends to increase steeply. With respect to $(St_{m2})_{av}$ at $i = 0°$, $(St_{m2})_{av}$ is reduced by 7.4% at $i = -10°$ and is augmented significantly by 38.7% at $i = 10°$. It should be noted that $(St_{m2})_{av}$ in Fig. 14 includes Reynolds number effects inevitably due to the fact that the value of $W_{2\infty}$ is different depending upon *i*. As mentioned earlier in Fig. 3, the turbine rotor blade passage is not a convergent channel any more when $i > 6.2°$, because the exit velocity is lower than the inlet one. $(St_{m1})_{av}$ is higher than $(St_{m2})_{av}$ when $i < 6.2°$ meanwhile $(St_{m1})_{av}$ is lower than $(St_{m2})_{av}$ when $i > 6.2°$.

6. Conclusions

Effects of incidence angle on the endwall convective transport within a high-turning turbine rotor cascade passage have been investigated. Surface flow visualizations and heat/mass transfer measurements are carried out at the inlet Reynolds number of 2.78×10^5 for incidence angles of −10°, −5°, 0°, 5°, and 10°. The results are summarized as follows.

(1) The incidence angle has considerable influences on the endwall local convective transport phenomena and on the behaviors of various endwall vortices.

(2) The surface flow visualizations show that in the case of negative incidence, there exists a considerable advancement of endwall separation line with a narrower suction-side corner vortex area, in comparison with the zero incidence case. In the case of positive incidence, there are a slight retreat and a minute advancement of the separation line near its ends with a wider suction-side corner vortex area.

(3) The mass transfer data provide that in the case of negative incidence, convective transport is less influenced by the leading edge horseshoe vortex and by the suction-side corner vortex along their loci but is increased along the pressure-side corner vortex. In the case of positive incidence, however, convective transport is augmented remarkably along the leading edge horseshoe vortex, and is much influenced by the suction-side corner vortex. Moreover, heat/mass transfer is enhanced significantly along the pressure-side leading edge corner vortex.

(4) Local endwall convective transport in the area other than the endwall vortex sites is much influenced by the inlet-to-exit velocity ratio in the cascade passage.

(5) With the increment of the incidence angle from −10° to 10°, mass transfer Stanton number averaged across the entire endwall region based on the inlet free-stream velocity decreases mildly but that based on the exit mid-span velocity increases more steeply.

References

[1] R.A. Oke, S.W. Burd, T.W. Simmon, R. Vahlberg, Measurements in a turbine cascade over a contoured endwall: discrete hole injection of bleed flow, ASME Paper No. 2000-GT-214 (2000).

[2] M.F. Blair, An experimental study of heat transfer and film cooling on large-scale turbine endwalls, ASME J. Heat Transfer 96 (1974) 524–529.

[3] R.A. Graziani, M.F. Blair, J.R. Taylor, R.E. Mayle, An experimental study of endwall and airfoil surface heat transfer in a large scale turbine blade cascade, ASME J. Eng. Power 102 (1980) 257–267.

[4] R.E. Gaugler, L.M. Russell, Comparison of visualized turbine endwall secondary flows and measured heat transfer pattern, ASME J. Eng. Gas Turbine Power 106 (1984) 168–172.

[5] R.E. York, L.D. Hylton, M.S. Mihelc, An experimental investigation of endwall heat transfer and aerodynamics in a linear vane cascade, ASME J. Eng. Gas Turbine Power 106 (1984) 159–167.

[6] R.J. Goldstein, R.A. Spores, Turbulent transport on the endwall in the region between adjacent turbine blades, ASME J. Heat Transfer 110 (1988) 862–869.

[7] P.W. Giel, D.R. Thurman, G.J.V. Fossen, S.A. Hippensteele, R.J. Boyle, Endwall heat transfer measurements in a transonic turbine cascade, ASME J. Turbomach. 120 (1998) 305–313.

[8] M.K.B. Kang, A. Kohli, K.A. Thole, Heat transfer and flowfield measurements in the leading edge region of a stator vane endwall, ASME J. Turbomach. 121 (1999) 558–568.

[9] M.K.B. Kang, K.A. Thole, Flowfield measurements in the endwall region of a stator vane, ASME J. Turbomach. 122 (2000) 458–466.

[10] R.W. Radomsky, K.A. Thole, High free-stream turbulence effects on endwall heat transfer for a gas turbine stator vane, ASME J. Turbomach. 122 (2000) 699–708.

[11] S.W. Lee, S.B. Jun, B.K. Park, J.S. Lee, Effects of combustor-level high inlet turbulence on the endwall flow and heat/mass transfer of a high-turning turbine rotor cascade, KSME Int. J. 18 (2004) 1435–1450.

[12] L.S. Langston, M.L. Nice, R.M. Hooper, Three-dimensional flow within a turbine cascade passage, ASME J. Eng. Power 99 (1977) 21–28.

[13] H.P. Hudson, R.G. Dominy, The off-design performance of a low pressure turbine cascade, ASME J. Turbomach. 109 (1987) 201–209.

[14] A. Yamamoto, Interaction mechanisms between tip-leakage flow and the passage vortex in a linear turbine rotor cascade, ASME J. Turbomach. 110 (1988) 329–338.

[15] A. Yamamoto, H. Nouse, Effects of incidence angle on three-dimensional flows in a linear turbine cascade, ASME J. Turbomach. 110 (1988) 486–496.

[16] A. Yamamoto, Endwall flow/loss mechanisms in a linear turbine cascade with blade tip clearance, ASME J. Turbomach. 110 (1987) 486–496.

[17] D.B.M. Jouini, S.A. Sjolander, S.H. Moustapha, Aerodynamic performance of a transonic turbine cascade at off-design conditions, ASME J. Turbomach. 123 (2001) 510–518.

[18] M.J. Brear, H.P. Hodson, N.W. Harvey, Pressure surface separations in low-pressure turbines-part 1: midspan behavior, ASME J. Turbomach. 124 (2002) 393–401.

[19] D.-H. Rhee, H.H. Cho, Local heat/mass transfer characteristics on a rotating blade with flat tip in a low-speed annular cascade-part I: near-tip surface, ASME J. Turbomach. 128 (2006) 96–109.

[20] D-H Rhee, H.H. Cho, Local heat/mass transfer characteristics on a rotating blade with flat tip in a low-speed annular cascade-part II: tip and shroud, ASME J. Turbomach. 128 (2006) 110–119.

[21] H. Cohen, G.F.C. Rogers, H.I.H. Saravanamuttoo, Gas Turbine Theory, Longman, Essex, 1995. pp. 319–320.

[22] D.G. Wilson, T. Korakianitis, The Design of High-Efficiency Turbomachinery and Gas Turbines, Prentice Hall, New Jersey, 1998. pp. 334–338.

[23] S.W. Lee, B.J. Chae, Effects of squealer rim height on aerodynamic losses downstream of a high-turning turbine rotor blade, Exp. Therm. Fluid Sci. 32 (2008) 1440–1447.

[24] S.W. Lee, Y.B. Kim, J.S. Lee, Flow characteristics and aerodynamic losses of film-cooling jets with compound angle orientations, ASME J. Turbomach. 119 (1997) 310–319.

[25] R.J. Goldstein, H.H. Cho, A review of mass transfer measurements using naphthalene sublimation, Exp. Therm. Fluid Sci. 10 (1995) 416–434.

[26] R.J. Goldstein, H.P. Wang, M.Y. Jabbari, The influence of secondary flows near the endwall and boundary layer disturbance on convective transport from a turbine blade, J. Turbomach. 117 (1995) 657–665.

[27] STP 470A, Manual on the Use of Thermocouples in Temperature Measurement, Published by ASTM, 1974.

[28] R.B. Abernethy, R.P. Benedict, R.B. Dowdell, ASME measurement uncertainty, ASME J. Fluids Eng. 107 (1985) 161–164.